Observation of an impurity hole in a plasma with an ion internal transport barrier in the Large Helical Device[a)]

K. Ida,[b)] M. Yoshinuma, M. Osakabe, K. Nagaoka, M. Yokoyama, H. Funaba, C. Suzuki,
T. Ido, A. Shimizu, I. Murakami, N. Tamura, H. Kasahara, Y. Takeiri, K. Ikeda,
K. Tsumori, O. Kaneko, S. Morita, M. Goto, K. Tanaka, K. Narihara, T. Minami,
I. Yamada, and LHD Experimental Group

National Institute for Fusion Sciences, Toki, Gifu 509-5292, Japan

Extremely hollow profiles of impurities (denoted as "impurity hole") are observed in the plasma with a steep gradient of the ion temperature after the formation of an internal transport barrier (ITB) in the ion temperature transport in the Large Helical Device [A. Iiyoshi *et al.*, Nucl. Fusion **39**, 1245 (1999)]. The radial profile of carbon becomes hollow during the ITB phase and the central carbon density keeps dropping and reaches 0.1%–0.3% of plasma density at the end of the ion ITB phase. The diffusion coefficient and the convective velocity of impurities are evaluated from the time evolution of carbon profiles assuming the diffusion and the convection velocity are constant in time after the formation of the ITB. The transport analysis gives a low diffusion of $0.1-0.2$ m^2/s and the outward convection velocity of ~ 1 m/s at half of the minor radius, which is in contrast to the tendency in tokamak plasmas for the impurity density to increase due to an inward convection and low diffusion in the ITB region. The outward convection is considered to be driven by turbulence because the sign of the convection velocity contradicts the neoclassical theory where a negative electric field and an inward convection are predicted. © *2009 American Institute of Physics*. [DOI: 10.1063/1.3111097]

I. INTRODUCTION

Simultaneous achievement of improved energy confinement and low impurity confinement is one of the crucial issues to realize the plasma relevant to nuclear fusion. Impurity accumulation has been a long-standing problem after the discovery of improved mode such as *H*-mode and internal transport barrier (ITB) because an impurity tends to accumulate in the plasma with an improved confinement. After the discovery of a high confinement mode (*H*-mode), strong impurity accumulation was observed in tokamaks.[1] However, since the edge localized mode (ELM) was found to prevent the impurity from penetrating into the core region of the plasma, the ELM was used to exhaust the impurity and avoid impurity accumulation. Another approach to avoid the impurity accumulation is to control the density profiles with an intensive gas puff, which has been demonstrated in high density *H*-mode plasmas in the Wendelstein 7-AS stellarator.[2] The decrease in a negative electric field contributes to prevent the impurity accumulation because the negative electric field tends to enhance the inward convection of impurities.[3] However, impurity accumulation is still a problem in discharges with an ITB (Ref. 4) because the strong negative electric field due to the steep pressure gradient in the ITB region causes the inward convection of impurities.[5] The inward convection in the ITB plasma would be a serious problem in the discharge where a high-*Z* gas (Ne or Ar) is injected to reduce the heat load to the divertor by enhancing the edge radiation. Because the high-*Z* impurity has strong accumulation[6] due to the *Z*-dependence of inward convection,[7,8] a very low impurity flux should be necessary to avoid the radiation and dilution due to impurities in the plasma with an ITB. Therefore, there is no compatibility between the ITB plasma and the edge radiation cooling scenario in tokamaks.

In neoclassical transport theory, a temperature screening effect due to an ion temperature gradient (ITG) is expected in tokamaks. In experiment, the outward convection of impurity was confirmed in the improved confinement plasma with a weak density gradient and a strong ITG.[9] On the other hand, in a nonaxisymmetric system there is no temperature screening because the outward convection due to the gradient of ion temperature is overcancelled by the inward convection due to the negative electric field, which is driven by the ITG.[10] However, in the nonaxisymmetric system, the impurity convection can be outward and the impurity density profile can be hollow due to the *positive* radial electric field in the electron-ITB plasmas, where the electron temperature is much higher than the ion temperature.[11] However, the inward convection of impurities is expected by neoclassical theory in plasmas with a high ITG because of the negative radial electric field. In this paper, extremely hollow impurity profiles and clear evidence of the outward convection of impurities in the plasma with a steep ITG in a nonaxisymmetric system are presented.

16, 056111-1

II. OBSERVATION OF IMPURITY HOLE

The Large Helical Device (LHD) is a heliotron-type device that has three high energy beams (180 keV) with negative ion sources (negative-neutral beam injection: N-NBI) for electron heating and one low energy beam (40 keV) with positive ion sources (positive-neutral beam injection: P-NBI) for ion heating. Both P-NBI and N-NBI are injected to the plasma with the magnetic field strength $B_0 = 2.68 - 2.79$ T, the position of the magnetic axis $R_{ax} = 3.55 - 3.7$ m, the pitch parameter $\gamma = 1.254$, and the canceling rate of the quadrupole field $B_q = 100\%$. The radial profiles of electron temperature and density are measured with a yttrium aluminum garnet (YAG) Thomson scattering system every 33 ms.[12] The radial profiles of the ion temperature and carbon density are measured with charge exchange spectroscopy (CXS) (Ref. 13) using the P-NBI as a probe beam. In order to subtract the background emission (cold component emitted from the plasma periphery) the beam power is modulated with 10 Hz (80 ms on, 20 ms off).

The carbon density is evaluated from the absolutely calibrated intensity of the charge exchange line of carbon CVI ($\Delta n = 8 - 7$) and the beam density calculated with the beam attenuation code based on the measured density and temperature profiles. While the direct charge exchange process between fully stripped impurity ions and neutral beam depends on relative velocity between the impurity and hydrogen atom of the beam, the cascade process is significantly affected by the distortion of the relative populations among the excited level ($n = 8$) of hydrogen-like impurity ions due to the l-mixing process.[14] Therefore, the charge exchange emission cross section, which determines the intensity of CVI line, depends on the surrounding plasma environment such as plasma density, ion temperature, and Z_{eff}. In this analysis the charge exchange emission cross section is calculated based on the measured plasma parameter using atomic data and analysis structure (ADAS).[15] The dependence of emission cross section on the surrounding plasma environment is relatively weak for the plasma parameters in this experiment. For example, after the transition from the L-phase to the ITB phase, the central ion temperature increases significantly (from 2 to 4 keV) but the change in the emission cross section is negligible (only 4% increase). Moreover the attenuation of the neutral beam in the plasma is moderate (one-third of the beam intensity is left even at the plasma center) because both the electron density and impurity concentration are relatively low [$n_e(0) \sim 1 \times 10^{19}$ m^{-3}, $n_C(0)/n_e(0) \sim 1\%$]. The beam intensity is strong enough even at the plasma center to evaluate accurate carbon density in the impurity hole. The impurity hole, which is characterized by the extremely hollow profile of the impurity density, is observed in the plasma with high ITG and is most pronounced in the plasma with an ion ITB.

Figure 1 shows the discharge with an impurity hole associated with the transition from the L-mode plasma to the plasma with an ion transport barrier (ITB). One P-NBI ($P_{abs} = 2$ MW) starts at $t = 1.5$ s with 10 Hz modulation (80 ms on, 20 ms off) to subtract the background of charge exchange line and the other three N-NBI ($P_{abs} = 10$ MW) are
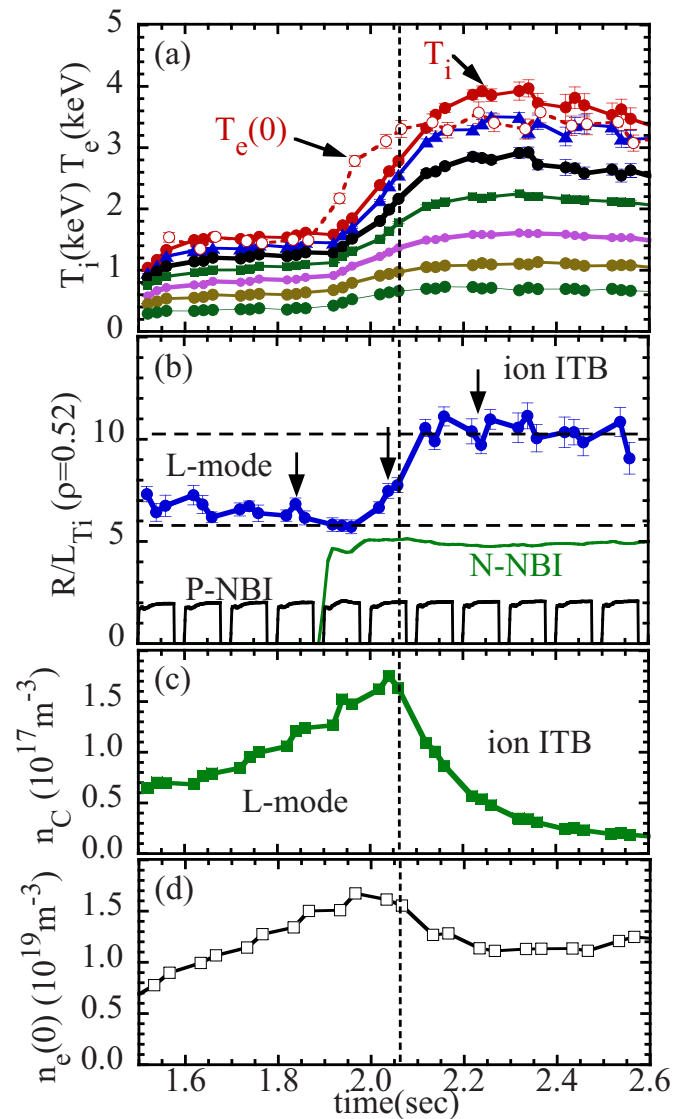

FIG. 1. (Color online) Time evolution of (a) central electron temperature and ion temperature at various radii, (b) normalized ITG R/L_{Ti}, where R is the major radius and L_{Ti} is the scale length of the ITG, and waveform of P-NBI (40 keV) and N-NBI (180 keV), (c) central carbon density, and (d) central electron density in the plasma with an ITB.

added at $t = 1.9$ s. Although 80% of the power of the P-NBI is deposited to ions, only 40% of the power of N-NBI is deposited to ions because the beam energy of N-NBI is high (180 keV). After the increase in NBI power, both the central electron and ion temperature increase. While the central electron temperature saturates at 0.2 s after the injection of the N-NBI, the central ion temperature keeps increasing after the saturation of the electron temperature and reaches up to 4 keV. This continuous increase in ion temperature is due to the transition from an L-mode plasma to the ITB plasma during the rise in the ion temperature. The ion temperature near the plasma edge tends to saturate earlier. In the ion ITB phase, the central ion temperature exceeds the central electron temperature, although the N-NBI contributes to electron heating rather than ion heating. Although the transition from the L-mode plasma to the ITB plasma is unclear in the time evolution of the ion temperature, the transition is clearly ob-

served in the time evolution of the normalized ITG, the so-called R/L_{Ti}, where R is the major radius and L_{Ti} is the scale length of the ITGs defined as $[(\partial Ti/\partial R)(\partial R/\partial \rho)/a]^{-1}$. The R/L_{Ti} value evaluated just inside the foot of the ITB (ρ =0.52) jumps from 6 to 10 at the transition from the L-mode to the ITB phase at t=2.06 s. The jump in the ITG is relatively small (a factor of 2), which is in contrast to the large jump in the electron temperature gradient (from ~5 to ~30) in the electron ITB plasmas.[11]

There are large varieties of radial profiles of temperature in the plasmas with an "ITB." For example, box-shaped ion temperature profiles are observed in the strong ITB plasmas with negative magnetic shear, while parabolic-shaped ion temperature profiles are observed in the weak ITB with positive magnetic shear in JT-60U tokamak.[16] The reduction in thermal diffusivity is large but it is localized in a relatively narrow region in the strong ITB, while the reduction in thermal diffusivity is moderate but it is expanded in the wide region in the plasma in the weak ITB. In the quiescent double barrier discharge in DIII-D,[17,18] which is also categorized to ITB discharge, the reduction in thermal diffusivity is observed in the very wide region in the plasma core. Therefore it is difficult to define the ITB by the size of the region of transport improvement because of the variety of radial profile of temperature. In order to solve this problem, a ratio of the major radius to the scale length of ion temperature R/L_{Ti} is proposed to be used to define the ITB when it exceeds the critical value.[19] In this paper, the term ITB is used to indicate the transport improvement in the interior plasma as demonstrated by the jump in R/L_{Ti} in Fig. 1(b) and the ITB is defined by the jump in R/L_{Ti} (jump to the large value which exceeds the critical value) not by the shape of ion temperature profile.

As seen in Fig. 1(c), the carbon density at the plasma center increases during the L-mode phase but it starts to decrease dramatically by an order of magnitude after the transition from the L-mode phase to the ion ITB phase. This is in contrast to the small decrease (only 30% drop) in the central electron density in the ion ITB phase. These data clearly show that the carbon impurity is strongly exhausted in the ITB phase. The carbon concentration is 1% in the L-mode phase but it starts to decrease after the transition from the L-mode phase to the ITB phase and finally it drops to 0.2% at the plasma center at 0.5 s after the transition.

The details of the time evolution of electron and ion temperature and electron and impurity density profiles are plotted in Fig. 2. The changes in profiles after the transition from the L-mode phase to the ITB phase are indicated by arrows. The electron temperature increases after the onset of N-NBIs (t=1.9 s) but it saturates in the time scale on the order of the global energy confinement time of ~40 ms. The shape of the electron temperature measured with the 136 spatial channel YAG Thomson scattering system is relatively broad and almost unchanged even after the formation of the ITB (t=2.06 s). The ion temperature profiles measured with a 50 spatial channel CXS system are as broad as electron temperature profiles in the L-mode phase and they become peaked at the plasma center along with the increase in the central ion temperature in the ITB phase (t>2.06 s). The
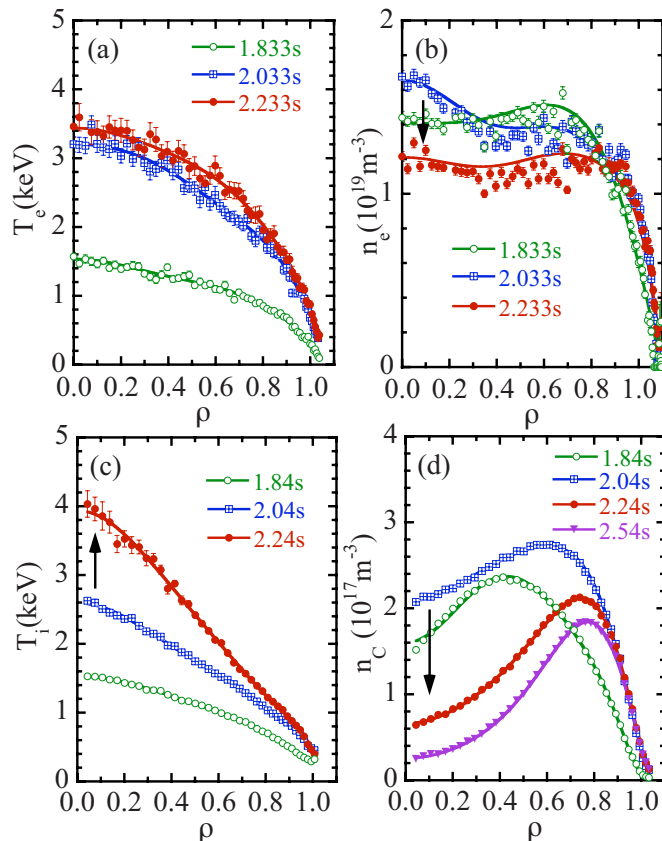

FIG. 2. (Color online) Radial profiles of (a) electron temperature, (b) electron density, (c) ion temperature, and (d) carbon density at the L-mode phase (t=1.84 s) just before the transition from the L-mode to the ITB phase (t=2.04 s) and at the ITB phase (t=2.24 s and t=2.54 s). The timing of the radial profiles measured is indicated with arrows in Fig. 1(b).

central ion temperature exceeds the central electron temperature and reaches 4 keV. In the ion ITB phase, the ITG at half of the plasma minor radius (ρ=0.5) is 5–6 keV/m, which is twice the electron temperature gradient. The significant differences in the profiles between the electron temperature and ion temperature indicate that there are clear differences in the heat transport between the electron and ion channels and the heat transport improvement appears only in the ion transport and not in the electron transport.

The electron density profiles are flat in the L-mode phase and in the ITB phase, while the profile becomes slightly peaked during the transient phase from the L-mode phase to the ITB phase. The carbon density profile is slightly hollow in the L-mode phase and it becomes extremely hollow in the ITB phase and the central carbon density keeps decreasing and reaches 0.2%–0.3% of the electron density at the plasma center. The central carbon concentration is one order of magnitude lower than the carbon concentration near the plasma periphery. The peak of the carbon density is located close to the plasma periphery at ρ=0.7–0.8 and the carbon density gradient becomes positive ($\partial n_C/\partial r > 0$) in the plasma core region of $\rho < 0.7$, where inward flux due to diffusion is almost balanced by the outward flux due to the strong outward convection velocity.

In these discharges there are no clear foot point observed in the radial profiles of ion temperature. However, the large
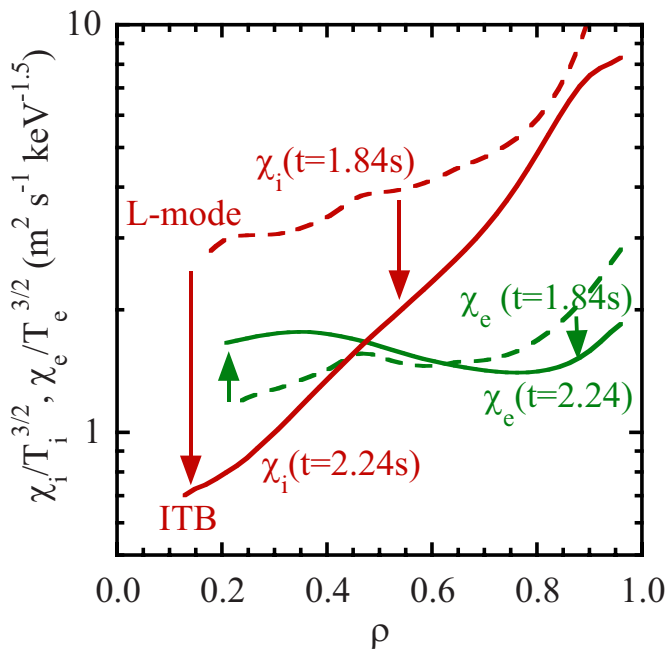
FIG. 3. (Color online) Radial profiles of ion and electron thermal diffusivity normalized by $T_i^{3/2}$ and $T_e^{3/2}$, respectively, at the *L*-mode phase ($t=1.84$ s) and ITB phase ($t=2.24$ s).

FIG. 4. (Color) Time evolution of (a) ion temperature at various radii ($\rho=0.03, 0.25, 0.43, 0.58, 0.74, 0.87, 0.98$), soft-x-ray image measured with a tangential x-ray CCD camera (b) before and (c) after the formation of the impurity hole, and (d) radial profiles of soft-x-ray intensity at the midplane.

increase in the ITG in the ITB phase ($t=2.24$ s) from that in the *L*-mode phase ($t=1.84$ s) clearly indicates the improvement of ion transport. In order to evaluate the improvement of ion transport quantitatively, the radial profiles of an ion and an electron thermal diffusivity are plotted in Fig. 3. Here the ion and electron thermal diffusivities are normalized by the gyro-Bohm factors $T_i^{3/2}$ and $T_e^{3/2}$ because the thermal diffusivity is proportional to $T^{3/2}$ in the gyro-Bohm transport in *L*-mode plasmas. In fact the normalized electron thermal diffusivity is almost unchanged after the formation of ion ITB because the electron transport is still in the level of the *L*-mode. However, the normalized ion thermal diffusivity drops by a factor of 4 near the plasma center and by a factor of 2 at a half of the plasma minor radius, which indicates a significant reduction in ion transport interior plasma after the formation of ITB. The reduction in ion thermal diffusivity is observed in the wide range in the plasma ($\rho<0.7$). The normalized ion thermal diffusivity is smaller than the normalized electron thermal diffusivity in the plasma core ($\rho<0.5$).

The impurity hole is also observed in the high-*Z* impurities as well as the low-*Z* impurity (carbon). Although there are no direct measurements of high-*Z* impurities, the radial profile of high-*Z* impurities can be inferred from the radial profiles of the soft-x-ray emission measured with the soft-x-ray charge coupled device (CCD) camera[20] and the vacuum ultraviolet (VUV) emission measured with the 20 spatial channel absolute extreme ultraviolet (AXUV) diode.[21] Figure 4 shows the time evolution of the ion temperature and the soft-x-ray image. The soft-x-ray image is measured with the soft-x-ray CCD camera with a tangential view at the beginning of the impurity hole formation [time A indicated in Fig. 4(a)] and the later time of the impurity hole (time B). The energy range measured with the soft-x-ray CCD camera is
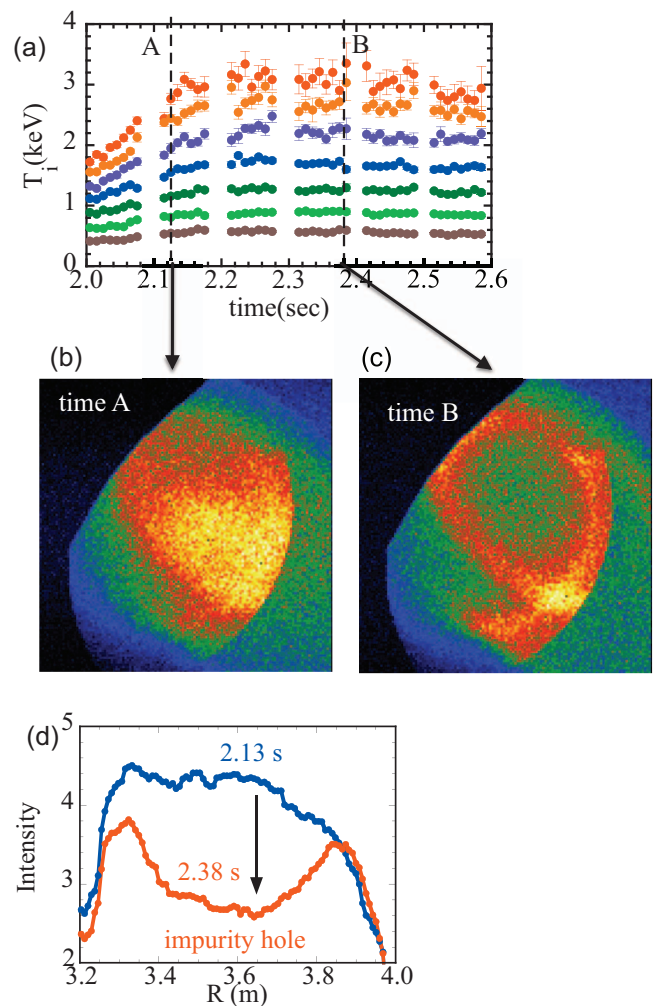
1–10 keV and $K\alpha$ lines of titanium, iron, and chromium have the dominant contributions. Therefore the soft-x-ray CCD camera is a useful tool to measure the two-dimensional radial distribution of high-*Z* impurities. The soft-x-ray image shows the drastic change in the impurity profile from centrally peaked to extremely hollow profiles. The radial profiles of soft-x-ray emission at the midplane are also plotted in Fig. 4(d). The intensity of soft-x-ray emission at the plasma center drops significantly while the emission near the plasma edge stays constant in time. These results clearly show that the impurity hole is observed both in the low-*Z* impurity (carbon) and in the high-*Z* impurity when the ITG becomes large enough.

Since neoclassical theory predicts outward flux in the plasma with a positive radial electric field when the electron temperature is higher than the ion temperature, it is interesting to compare the discharges with different T_e/T_i ratio. Figure 5 shows the time evolution of the central electron temperature and ion temperature and carbon density in the discharges with the N-NBI power of 16 MW and with the N-NBI power stepped down to 6 MW. The central ion temperature increases up to 3.6 keV in the discharge with higher
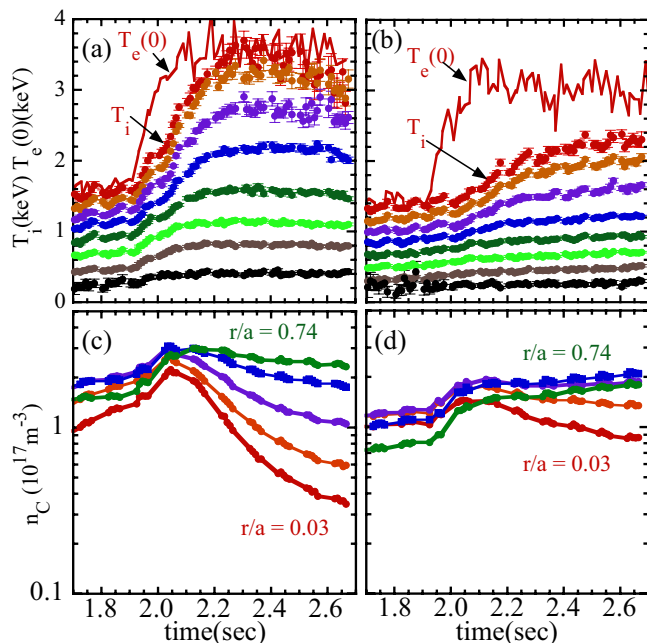
FIG. 5. (Color online) Time evolution of [(a) and (b)] central electron temperature and ion temperature at various radii ($\rho=0$, 0.13, 0.37, 0.50, 0.66, 0.81, 0.93, 1.0) in the discharge (a) with and (b) without an ion ITB and time evolution of [(c) and (d)] carbon density at various radii ($\rho=0.03, 0.25, 0.43, 0.58, 0.74$) in the discharge (c) with and (d) without an ion ITB.
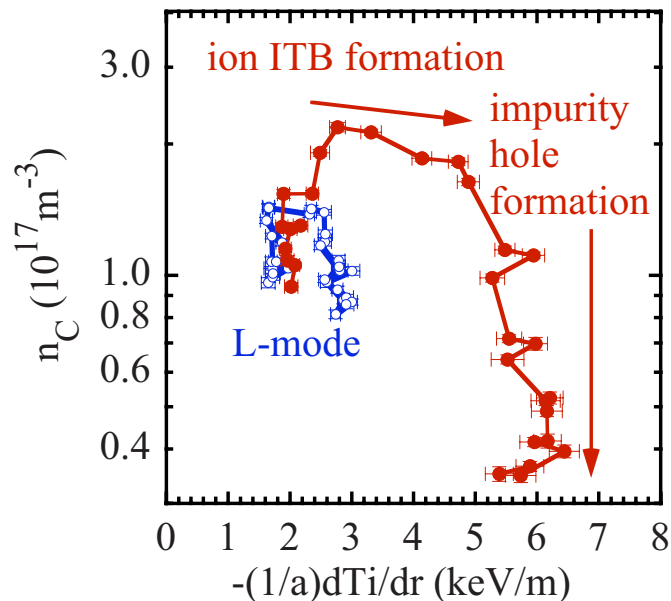

FIG. 6. (Color online) Relation between central carbon density and temperature gradient at $\rho=0.6$ for the *L*-mode discharge and ITB discharge. The data are plotted every 20 ms.

NBI power, while it increases only up to 2.3 keV in the discharge with lower NBI power. The ITG $\partial T_i/\partial r$ in the core region of the plasma in the discharge with higher N-NBI power is almost twice that of the discharge with lower N-NBI power. It should be noted that the T_e/T_i ratio is even lower in the discharge with higher N-NBI power. Since the power of the N-NBI is deposited to electron more than to ions, the T_e/T_i ratio should increase as the N-NBI power is increased if the electron and ion heat transports are unchanged. Therefore the increase in ion temperature (decrease in T_e/T_i ratio) with higher N-NBI power is due to the improvement of the ion transport.

As seen in Figs. 5(c) and 5(d), the carbon density near the plasma periphery starts to increase at the onset of N-NBI at $t=1.9$ s. This is because of the increasing carbon influx from the NBI armor. On the other hand, the carbon density at the plasma center ($\rho=0.03$) decreases almost by an order of magnitude in the plasma with higher ion temperature (lower T_e/T_i ratio), while the central carbon density decreases slightly and goes back to the level before the NBI in the discharge with lower ion temperature (higher T_e/T_i ratio). It should be noted that the carbon density keeps decreasing as long as the ion temperature is high. The decay time of the carbon density is very long ($\sim$0.2 sec) compared with the energy confinement time ($\sim$0.04–0.05 s), which implies that the diffusion coefficient of impurity transport is very low. These results clearly show that the formation of an impurity hole is related to the increase in ion temperature and not the electron or T_e/T_i ratio and contradicts the neoclassical prediction.

The relation between the ITG at half of the plasma minor radius of $\rho=0.6$ and the central carbon density is plotted in Fig. 6. In the *L*-mode discharge with low N-NBI power, the ITG is below 3 keV/m and the central carbon density is $\sim1\times10^{17}$ m^{-3}, which is 1% of the electron density. In the discharge with an ion ITB, the ITG increases to 5 keV/m after the formation of the ion ITB and the impurity hole formation starts. Associated with the further increase in the ITG of up to 6 keV/m, the central carbon density drops to $\sim3\times10^{16}$ m^{-3}, which is only 0.3% of the electron density. It should be noted that the trajectory of the data points indicates that the ion ITB formation precedes the impurity hole formation.

III. IMPURITY TRANSPORT ANALYSIS

The radial particle flux of carbon Γ_c and the density gradient of carbon are calculated from the time slices of the carbon density profiles. The particle flux of the impurity Γ_I (I=C for carbon) at r in minor radius is given as

$$\Gamma_I(r) = \frac{1}{r}\int_0^r r'\left[S(r') - \frac{dn_I(r')}{dt}\right]dr'. \tag{1}$$

Here the source term S can be neglected in this experiment because the source of carbon is localized near the plasma edge and there is no impurity source in the plasma core region of $\rho<0.9$. It is well known that there is a significant contribution by off-diagonal terms of the transport matrix[22] in the particle transport, and the radial particle flux of the impurity normalized by the density can be written as a sum of diffusive (diagonal) terms and nondiffusive (off-diagonal) terms as

$$\frac{\Gamma_I}{n_I} = -D\frac{\nabla n_I}{n_I} + V, \tag{2}$$

where D is the diffusion coefficient, V is the convection velocity, positive V stands for outward convection, and negative V stands for inward convection (inward pinch), which is typically observed in tokamak plasmas.[23,24] The diffusion coefficient and the convective velocity can be evaluated from the time evolution of carbon profiles assuming the diffusion and the convection velocity are constant in time after the formation of the ITB. The diffusion coefficient and convection velocity can be evaluated by a linear fit of the particle flux normalized by the density and the density gradient normalized by the density. This analysis requires a significant change in density gradients to evaluate the diffusion coefficient accurately. Therefore the diffusion coefficients cannot be evaluated in L-mode plasmas where the change in the density gradient is relatively small.

Figure 7(a) shows the carbon radial flux normalized by its density as a function of the carbon density gradient normalized by its density and radial profiles during the decay phase of carbon density after the formation of the ion ITB ($t=2.19–2.49$ s). The relation between the normalized flux and the normalized density gradient is linear at various radii in the plasma, which clearly shows the validity of the assumption that the diffusion coefficient and the convection velocity are constant in time during the decay phase. Because of the hollow profile of the carbon density, the normalized carbon density gradient is positive except for the region near the plasma edge. The offset of the normalized flux at zero gradient is positive, which indicates that the convection velocity is positive (outward convection) in the plasma core ($\rho<0.75$).

Figures 7(b) and 7(c) show the radial profiles of the diffusion coefficient and convection velocity derived from the slope and offset of the data points during the decay phase (2.19–2.49 s) in Fig. 7(a). The diffusion coefficient is 0.1–0.2 m^2/s in the plasma core ($\rho<0.5$), which is twice the neoclassical prediction and increases sharply toward the plasma edge. The diffusion coefficient exceeds 1 m^2/s near the plasma periphery. The convection velocity estimated from Fig. 7(a) is positive in the core region ($\rho<0.78$), which indicates outward convection, while it becomes negative (inward convection) near the plasma periphery ($\rho>0.8$). The outward convection velocity in the plasma core and inward convection near the plasma periphery can produce the hollow carbon density profiles peaked at $\rho\sim0.8$, as seen in Fig. 2(d).

It is important to compare the diffusion coefficient and convection velocity measured with the neoclassical prediction to investigate the mechanism of formation of the impurity hole. The radial electric field is calculated with the ambipolar condition of neoclassical radial fluxes of electron and ion. The electron and ion radial fluxes and consistent radial electric field are calculated based on the measured radial profiles of electron and ion temperature and electron and carbon density using the GSRAKE code.[25] In the neoclassical theory, the normalized particle flux of the impurity Γ_I/n_I can be expressed as
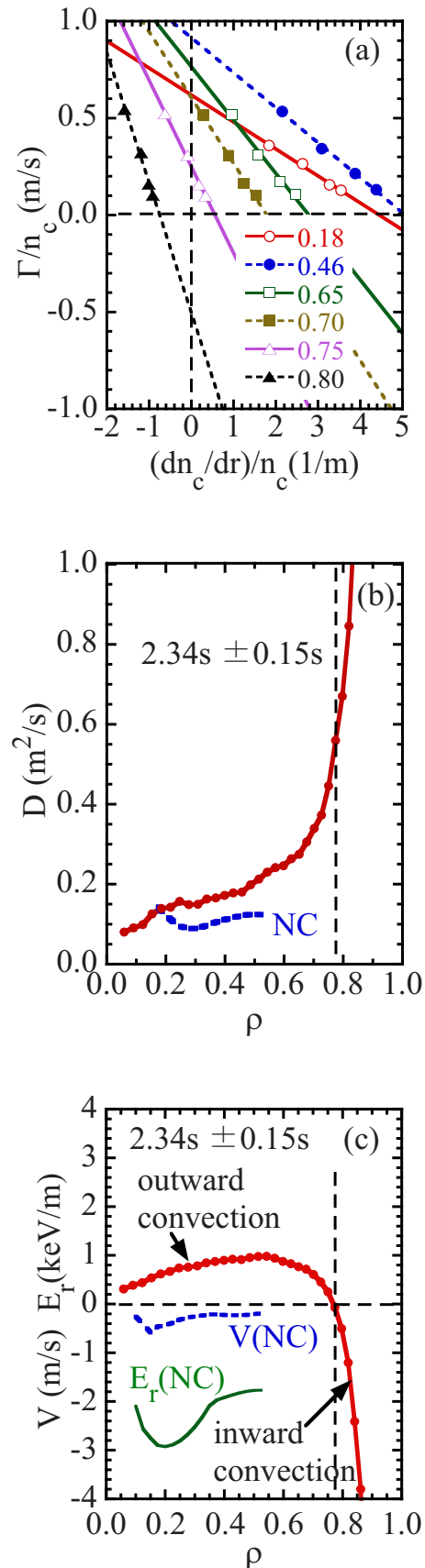

FIG. 7. (Color online) (a) Carbon radial flux normalized by its density as a function of carbon density gradient normalized by its density and radial profiles of (b) diffusion coefficient and (c) convection velocity and predicted radial electric field. The closed circles in (b) and (c) are experimental data and the dashed lines are neoclassical predictions.

$$\frac{\Gamma_I}{n_I} = -D_1 \left[\frac{\nabla n_I}{n_I} + \frac{q_I \nabla \Phi}{kT_i} + \left(\frac{D_2}{D_1} - \frac{3}{2} \right) \frac{\nabla T_i}{T_i} \right], \quad (3)$$

where D_n are neoclassical transport coefficients given by the energy integration of the diffusion coefficient[26] as

$$D_n = \frac{2}{\sqrt{\pi}} \int_0^\infty x_j^{(n-0.5)} D(x_j) e^{-x_j} dx_j, \quad (4)$$

where

$$x_j = \frac{m_j v_j^2}{2kT_j}. \quad (5)$$

Here k is the Boltzmann constant, m_j is the mass of ion species j, v_j is the velocity of ion species j, and q_j is the charge of the ion of interest and is six for carbon. In the parameter regime in this experiment, the ratio of diffusion coefficients $D_2/D_1 = 2.5$–3.0. Since the $\nabla \Phi/(k \nabla T_i) \sim 1$ in the ion root (negative electric field regime), the radial electric field term (second term) is 4–6 times larger than the temperature screening term (third term). The radial electric field term is negative (inward convection) for negative electric field and the temperature screening term is always positive (outward convection).

Because of the low concentration of central carbon density due to the formation of impurity hole, the measurements of poloidal flow using CXS are not available near the plasma center because of the non-negligible integration effect of the measurements along the line of sight within finite beam width. (The ion temperature and carbon density presented in this paper are measured with the CXS with toroidal view, which has much less integration effect.) Alternatively, the radial electric field can be measured with a heavy ion beam probe (HIBP).[27] The radial electric field measured with the HIBP in a similar discharge shows it is negative (~ 3 kV/m) near the plasma center at $\rho = 0.2$, which is consistent with that predicted by neoclassical theory in this discharge. The convection velocity predicted by the neoclassical theory is negative in the ion root in a nonaxisymmetric system because the temperature screening effect is masked by the inward pinch due to the negative electric field. This is in contrast to the situation where there are no radial electric field terms and the temperature screening effect is expected to contribute to the impurity exhaust in tokamak neoclassical theory. Since neoclassical theory fails to explain the outward convection observed in the impurity hole, the outward convection velocity evaluated from the time evolution of the carbon density profiles should be driven by turbulence.

IV. MAGNETIC AXIS DEPENDENCE OF TRANSPORT COEFFICIENTS

The strength of the impurity hole depends on the configuration of the magnetic field, especially the position of the magnetic axis. The impurity hole becomes stronger as the magnetic axis is shifted outward. As the magnetic axis is shifted outward, the radial electric field changes its structure.[28] The radial electric field tends to be more positive for the outward shift, where the impurity hole becomes strong and neoclassical transport becomes dominant. Al-
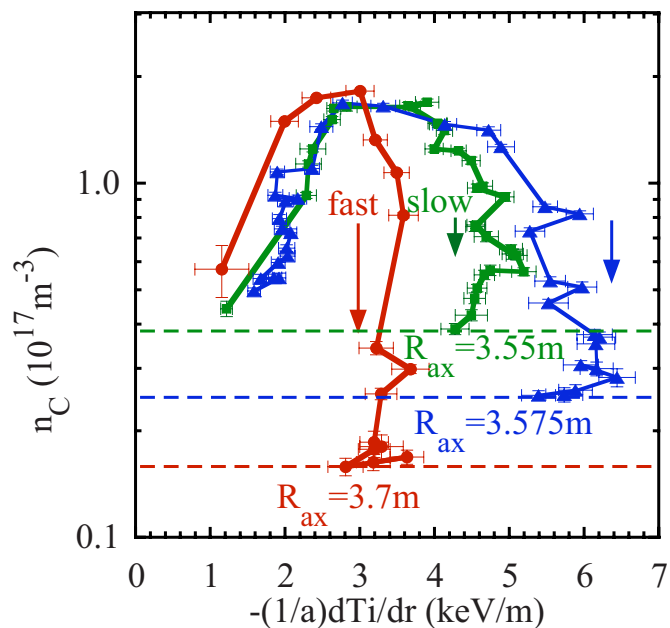

FIG. 8. (Color online) Relation between central carbon density and temperature gradient at $\rho = 0.6$ in discharges with different magnetic axes.

though the stronger impurity hole in the outer shifted configuration may be qualitatively consistent with the neoclassical prediction, the sign and magnitude of the convection velocity observed do not agree with the neoclassical prediction.

As seen in Fig. 8, the speed of the decrease in the carbon density after the impurity hole formation strongly depends on the magnetic axis position. As the magnetic axis moves outward from 3.55 to 3.7 m, the speed of the carbon density drop becomes faster and the final carbon density level becomes lower. The impurity density drops to 5×10^{16} m^{-3} in the configuration of $R_{ax} = 3.55$ m, which is similar to the level of the carbon concentration before the NBI, while it drops to 1.5×10^{16} m^{-3} in the configuration of $R_{ax} = 3.7$ m, which is only $\sim 0.1\%$ of the central electron density. The formation of the impurity hole starts when the ITG reaches a critical value and the critical value is 6 keV/m in the plasma with the inner shifted configuration of $R_{ax} = 3.55$ m, while it is only 3 keV/m in the plasma with the outer shifted configuration of $R_{ax} = 3.7$ m.

The differences in impurity hole formation are also clearly observed in the time evolution of radial profiles of carbon density, as seen in Fig. 9. In the plasma with an inner shifted configuration of $R_{ax} = 3.55$ m, the central carbon density drops to the level of one third of the carbon density at the peak at $\rho = 0.6$. As the magnetic axis moves outward, the hollowness of the carbon density becomes large and the central carbon density is one tenth of the peak carbon density at $\rho = 0.8$ at the most outward shifted configuration of $R_{ax} = 3.7$ m. It should be noted that the carbon density near the periphery region $\rho > 0.8$ is almost unchanged in time, which indicates that the carbon influx is also unchanged. The strong hollowness and fast drop in the central carbon density in the discharge with an outer shifted configuration are due to the larger convection velocity in the core region. The radial
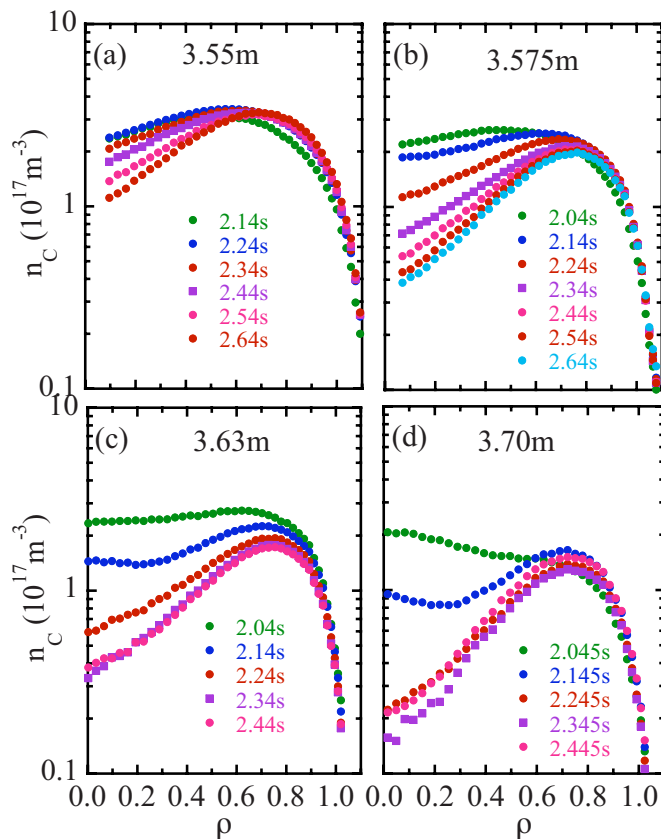
FIG. 9. (Color online) Time evolution of radial profiles of carbon density in plasmas with magnetic axes of (a) 3.55, (b) 3.575, (c) 3.63, and (d) 3.70 m.
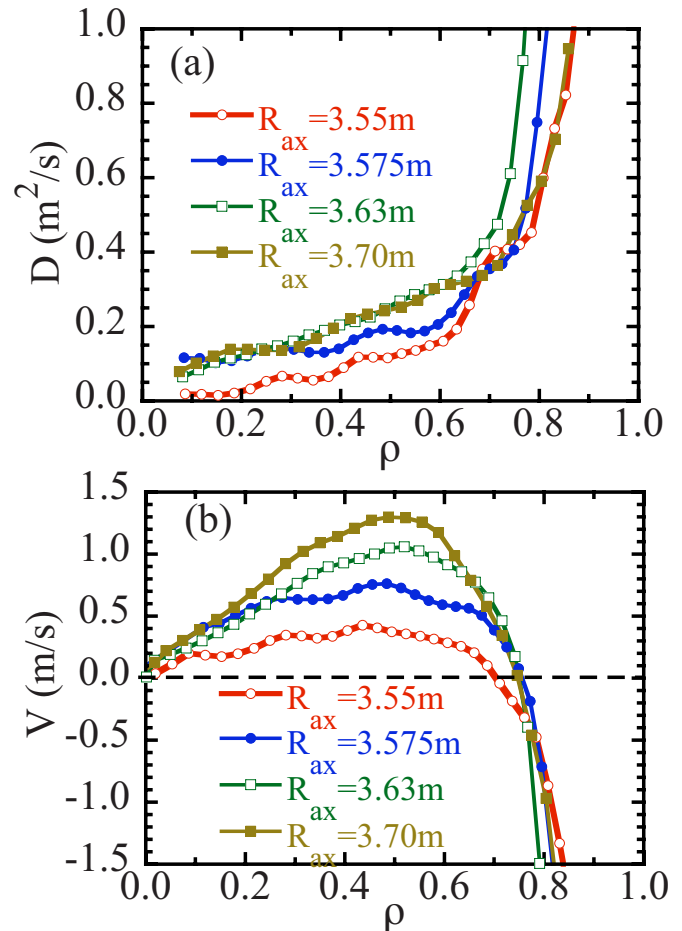

FIG. 10. (Color online) Radial profiles of (a) diffusion coefficients and (b) convection velocity in plasmas with magnetic axes of 3.55, 3.575, 3.63, and 3.70 m.

profiles of the diffusion coefficient and the convection velocity are evaluated from the time evolution of the carbon density profiles. As seen in Fig. 10, the diffusion coefficients near the plasma center are ~ 0.1 m^2/s in the discharge with $R_{ax} = 3.575$, 3.6, and 3.70 m and they increase toward the plasma periphery. Although the diffusion coefficients are more or less unchanged except for the discharge with $R_{ax} = 3.55$ m, the convection velocity strongly depends on the magnetic axis position. The convection velocity is positive in the plasma core and has a peak at $\rho = 0.5$. The peak value is 0.4 m/s in the inner shifted configuration while it is 1.2 m/s in the outer shifted configuration. In this configuration, the convection velocity changes its sign at $\rho = 0.7$ and is negative (inward convection) near the plasma periphery.

V. DISCUSSIONS

The extremely hollow profile of the carbon impurity is observed in plasma with a steep gradient of the ion temperature (5–6 keV/m). Transport analysis shows the low diffusion coefficient of the carbon impurity of 0.1 m^2/s in the plasma core and the large positive convection velocity of ~ 1 m/s of the impurity driven by the ITG, which is considered to be driven by turbulence because the sign of the convection velocity contradicts the neoclassical prediction. It should be noted that experimental data clearly show outward convection (positive V), of which the sign of the convection velocity is opposite to that predicted by neoclassical theory (negative V). Therefore the outward convection observed in

LHD is considered to be driven by turbulence. One of the candidates for driving the outward convection is the ITG mode because the strong correlation between the outward convection and the ITG is observed.

The similar transport analysis was done for bulk ions based on the time evolution of bulk ions estimated from the electron density and carbon density profile and particle source due to fueling from the neutral beam. The diffusion coefficient of bulk ion is almost identical to that of impurity ions; however, the convection velocity of bulk ion is close to zero and much smaller than the impurity ions. It is not clear why only the impurity has a strong outward convection and not the bulk ions. Furthermore the outward convection velocity in the core region increases as the magnetic axis moves outward. Although the neoclassical contribution to the transport becomes larger as the magnetic axis moves outward, the neoclassical convection does not contribute to produce outward convection (in fact it contributes to inward convection). The magnetic axis dependence of the convection velocity is also not understood yet. In order to investigate the physics mechanism of the impurity hole, the turbulence measurements should be necessary and are planned to be installed in LHD.

It is also interesting that the observation of the impurity hole in LHD is in contrast to the impurity accumulation in

ITBs in tokamaks,[29,30] where the temperature screening effect is canceled by the inward convection driven by the density gradient due to the improvement of particle transport. The experimental observation of the outward convection driven by the ITG should have a strong impact on the prospect of future research in nonaxisymmetric systems because it strongly supports the simultaneous achievement of good energy confinement and low impurity concentration, which is necessary for a fusion plasma.

ACKNOWLEDGMENTS

[1] K. Ida, R. J. Fonck, S. Sesnic, R. A. Hulse, B. LeBlanc, and S. F. Paul, Nucl. Fusion **29**, 231 (1989).

[2] K. McCormick, P. Grigull, R. Burhenn, R. Brakel, H. Ehmler, Y. Feng, F. Gadelmeier, L. Giannone, D. Hildebrandt, M. Hirsch, R. Jaenicke, J. Kisslinger, T. Klinger, S. Klose, J. P. Knauer, R. Konig, G. Kuhner, H. P. Laqua, D. Naujoks, H. Niedermeyer, E. Pasch, N. Ramasubramanian, N. Rust, F. Sardei, F. Wagner, A. Weller, U. Wenzel, and A. Werner, Phys. Rev. Lett. **89**, 015001 (2002).

[3] K. Ida, R. Burhenn, K. McCormick, E. Pasch, H. Yamada, M. Yoshinuma, S. Inagaki, S. Murakami, M. Osakabe, Y. Liang, R. Brakel, H. Ehmler, L. Giannone, P. Grigull, J. P. Knauer, H. Maassberg, and A. Weller, Plasma Phys. Controlled Fusion **45**, 1931 (2003).

[4] Y. Koide, M. Kikuchi, M. Mori, S. Tsuji, S. Ishida, N. Asakura, Y. Kamada, T. Nishitani, Y. Kawano, T. Hatae, T. Fujita, T. Fukuda, A. Sakasai, T. Kondoh, R. Yoshino, and Y. Neyatani, Phys. Rev. Lett. **72**, 3662 (1994).

[5] R. Dux, C. Giroud, K.-D. Zastrow, and JET EFDA Contributors, Nucl. Fusion **44** 260 (2004).

[6] H. Kubo, S. Sakurai, S. Higashijima, H. Takenaga, K. Itami, S. Konoshima, T. Nakano, Y. Koide, N. Asakura, K. Shimizu, T. Fujita, and K. W. Hill, J. Nucl. Mater. **313–316**, 1197 (2003).

[7] K. Ida, R. J. Fonck, S. Sesnic, R. A. Hulse, and B. LeBlanc, Phys. Rev. Lett. **58**, 116 (1987).

[8] R. Dux, A. G. Peeters, A. Gude, A. Kallenbach, R. Neu, and ASDEX Upgrade Team, Nucl. Fusion **39**, 1509 (1999).

[9] M. R. Wade, W. A. Houlberg, and L. R. Baylor, Phys. Rev. Lett. **84**, 282 (2000).

[10] Y. Igitkhanov, E. Polunovsky, C. D. Beidler, R. Burhenn, and K. Yamazaki, J. Plasma Fusion Res. **7**, 89 (2006).

[11] K. Ida, T. Shimozuma, H. Funaba, K. Narihara, S. Kubo, S. Murakami, A. Wakasa, M. Yokoyama, Y. Takeiri, K. Y. Watanabe, K. Tanaka, M. Yoshinuma, Y. Liang, and N. Ohyabu, and LHD Experimental Group, Phys. Rev. Lett. **91**, 085003 (2003).

[12] K. Narihara, I. Yamada, H. Hayashi, and K. Yamauchi, Rev. Sci. Instrum. **72**, 1122 (2001).

[13] K. Ida, S. Kako, and Y. Liang, Rev. Sci. Instrum. **71**, 2360 (2000).

[14] R. J. Fonck, D. S. Darrow, and K. P. Jaehnig, Phys. Rev. A **29**, 3288 (1984).

[15] H. P. Summers and M. G. O'Mullane, AIP Conf. Proc. **543**, 304 (2000); H. P. Summers, N. R. Badnell, M. G. O'Mullane, A. D. Whiteford, R. Bingham, B. J. Kellett, J. Lang, K. H. Behringer, U. Fantz, K.-D. Zastrow, S. D. Loch, M. S. Pindzola, D. C. Griffin, and C. P. Balance, Plasma Phys. Controlled Fusion **44**, B323 (2002).

[16] Y. Sakamoto, T. Suzuki, S. Ide, Y. Koide, H. Takenaga, Y. Kamada, T. Fujita, T. Fukuda, T. Takizuka, H. Shirai, N. Oyama, Y. Miura, JT-60 Team, K. W. Hill, and G. Rewoldt, Nucl. Fusion **44**, 876 (2004).

[17] E. J. Doyle, L. R. Baylor, K. H. Burrell, T. A. Casper, J. C. DeBoo, D. R. Ernst, A. M. Garofalo, P. Gohil, C. M. Greenfield, R. J. Groebner, A. W. Hyatt, G. L. Jackson, T. C. Jernigan, J. E. Kinsey, L. L. Lao, C. J. Lasnier, J.-N. Leboeuf, M. Makowski, G. R. McKee, R. A. Moyer, M. Murakami, T. H. Osborne, W. A. Peebles, M. Porkolab, G. D. Porter, T. L. Rhodes, J. C. Rost, D. Rudakov, G. M. Staebler, B. W. Stallard, E. J. Strait, R. D. Sydora, E. J. Synakowski, M. R. Wade, G. Wang, J. G. Watkins, W. P. West, and L. Zeng, Plasma Phys. Controlled Fusion **43**, 95 (2001).

[18] G. Q. Li, S. J. Wang, L. L. Lao, A. D. Turnbull, M. S. Chu, D. P. Brennan, R. J. Groebner, and L. Zha, Nucl. Fusion **48**, 015001 (2008).

[19] R. C. Wolf, Plasma Phys. Controlled Fusion **45**, R1 (2003).

[20] C. Suzuki, K. Ida, T. Kobuchi, M. Yoshinuma, and LHD Experimental Group, Rev. Sci. Instrum. **79**, 10E929 (2008).

[21] B. J. Peterson, A. Yu. Kostrioukov, N. Ashikawa, Y. Liu, Y. Xu, M. Osakabe, K. Y. Watanabe, T. Shimozuma, S. Sudo, and LHD Experiment Group, Plasma Phys. Controlled Fusion **45**, 1167 (2003).

[22] S.-I. Itoh, Phys. Fluids B **4**, 796 (1992).

[23] A. A. Ware, Phys. Rev. Lett. **25**, 15 (1970).

[24] P. W. Terry, Phys. Fluids B **1**, 1932 (1989).

[25] C. D. Beidler and W. D. D'haeseleer, Plasma Phys. Controlled Fusion **37**, 463 (1995).

[26] A. A. Galeev and R. Z. Sagdeev, Rev. Plasma Phys. **7**, 307 (1977).

[27] T. Ido, A. Shimizu, M. Nishiura, A. Nishizawa, S. Kato, T. P. Crowley, K. Tsukada, M. Yokota, H. Ogawa, T. Inoue, Y. Hamada, and LHD Experimental Group, Rev. Sci. Instrum. **77**, 10F523 (2006).

[28] K. Ida, M. Yoshinuma, M. Yokoyama, S. Inagaki, N. Tamura, B. J. Peterson, T. Morisaki, S. Masuzaki, A. Komori, Y. Nagayama, K. Tanaka, K. Narihara, K. Y. Watanabe, C. D. Beidler, and LHD Experimental Group, Nucl. Fusion **45**, 391 (2005).

[29] H. Chen, N. C. Hawkes, L. C. Ingesson, N. J. Peacock, and M. G. Haines, Nucl. Fusion **41**, 31 (2001).

[30] H. Takenaga, S. Higashijima, N. Oyama, L. G. Bruskina, Y. Koide, S. Ide, H. Shirai, Y. Sakamoto, T. Suzuki, K. W. Hill, G. Rewoldt, G. J. Kramer, R. Nazikian, T. Takizuka, T. Fujita, A. Sakasai, Y. Kamada, H. Kubo, and JT-60 Team, Nucl. Fusion **43**, 1235 (2003).